Band Alignment of Sputtered and Atomic Layer Deposited SiO_2 and Al_2O_3 on ScAlN

Xinyi Xia[1], Jian-Sian Li [1], Md Irfan Khan[2], Kamruzzaman Khan[2], Elaheh Ahmadi[2], David C. Hays[3], Fan Ren[1] and S.J. Pearton[4]

[1] Department of Chemical Engineering, University of Florida, Gainesville, FL 32611 USA

[2] Department of Electrical Engineering and Computer Science, University of Michigan, Ann Arbor, MI 48109 USA

[3] Nanoscale Research Facility, University of Florida, Gainesville, FL 32611 USA

[4] Department of Materials Science and Engineering, University of Florida, Gainesville, FL 32611 USA

Abstract

The band alignments of two candidate dielectrics for ScAlN, namely SiO_2 and Al_2O_2, were obtained by X-ray photoelectron spectroscopy (XPS). We compared the effect of deposition method on the valence band offsets of both sputtered and atomic layer deposition (ALD) films of SiO_2 and Al_2O_3 on $Sc_{0.27}Al_{0.73}$ N (bandgap 5.1 eV) films. The band alignments are type I (straddled gap) for SiO_2, type II (staggered gap) for Al_2O_3. The deposition methods make a large difference in relative valence band offsets, in the range 0.4-0.5 eV for both SiO_2 and Al_2O_3. The absolute valence band offsets were 2.1 or 2.6 eV for SiO_2 and 1.5 or 1.9 eV for Al_2O_3 on the ScAlN. Conduction band offsets derived from these valence band offsets, and the measured bandgaps were then in the range 1.0-1.1 eV for SiO_2 and 0.30-0.70 eV for Al_2O_3. These latter differences can be partially ascribed to changes in bandgap for the case of SiO_2 deposited by the two different methods, but not for Al_2O_3, where the bandgap as independent of deposition method. Since both dielectrics can be selectively removed from the ScAlN, they are promising as gate dielectrics for transistor structures.

Introduction

Recent advances in the growth of ScAlN by molecular beam epitaxy (MBE) (1-3) and metal organic chemical vapor deposition (MOCVD) (4,5) have led to significant renewed interest for its use in high frequency, thin film, surface acoustic wave (SAW) resonators (6-15) and ferroelectric memories (16). The improved purity and crystalline quality of these films lead to improved ferroelectric switching characteristics compared to previous sputter-deposited films (6). AlScN alloys with a high concentration of scandium can significantly improve the piezoelectric properties relative to the more common AlN piezoelectric films used in micro-electromechanical systems (MEMS), such as acoustic resonators for sensor and actuator applications (1-7). The Sc enhances the spontaneous polarization in hexagonal AlN and increases the piezoelectric and pyroelectric coefficients (15-20). The AlScN/GaN heterostructure has also been used for high electron mobility transistors (HEMTs) with excellent dc and rf characteristics (21-23). In that case, the typical Sc mole fraction is typically in the range 17-25% (2).

A key requirement for any advanced device application is to have dielectric films for ScAlN that provide carrier confinement in heterojunctions, surface passivation and can be selectively patterned or removed without damaging the ScAlN. Two of the most promising dielectrics for ScAlN are SiO_2 and Al_2O_3, due to their well-developed deposition processes and their large bandgaps. SiO_2 has a band gap of ~8.7 eV, which is a prerequisite for achieving large valence and conduction band offsets, blocking hole and electron transfer. Although Al_2O_3 (~6.3 eV) has a smaller band gap than SiO_2, its dielectric constant is higher, making it advantageous in various applications. For devices such as ScAlN metal-oxide-semiconductor field effect transistors (MOSFETs), the integration of higher dielectric constant (κ) materials in the gate structure can lower the effect of interface defects, lower the device's power consumption, and increase the capacitance density of the gate oxide.

In this paper, we report the band alignment on ScAlN of these two dielectrics, namely SiO_2 and Al_2O_3, which were each deposited by two different methods-sputtering or atomic layer deposition (ALD). The band alignments are type I (straddled gap) for SiO_2, type II (staggered gap) for Al_2O_3. The magnitude of the valence and conduction band offsets depends on the dielectric deposition method. This shows that careful attention must be paid to the process integration of these dielectrics with ScAlN to optimize the quality of the heterointerfaces between this material and the dielectrics.

Experimental

The ScAlN sample was grown on a Veeco GENXplore MBE system with conventional Al, Ga and Sc effusion cells and a radiofrequency (RF) plasma source to supply active nitrogen. The N source consisted of ultrahigh-purity (99.9995%) N_2 gas flowing at 1 SCCM through the rf-plasma source with 350-W rf power, which corresponded to a growth rate of ~6 nm/min for metal rich GaN layers. Commercially available on axis semi-insulating Ga polar GaN on sapphire substrate was used for the growth of $Sc_{0.27}Al_{0.73}N$. Before the growth, the substrate was coated with 500nm of e-beam evaporated Ti on the backside to ensure uniform heating by the substrate heater. Then the substrate was exposed to the ultra-violet (UV) ozone and diluted buffered hydrofluoric acid (BHF) etching to remove possible polishing damages and impurities from the substrate surface. After that the substrate was solvent cleaned with 4 minutes soak of acetone, methanol and isopropanol to remove all the organic residues from substrate surface. After cleaning, the substrate piece was bonded to a Si wafer with molten In. The prepared substrate was then loaded into the MBE load lock chamber. An hour of baking was performed at 400 °C in the buffer chamber to remove any water prior to transferring the substrate to the growth chamber. During the growth the substrate temperature was measured and monitored using the thermocouple. The growth was monitored in situ via reflection high-energy electron diffraction (RHEED).

The growth was initiated by 5 cycle of Ga deposition and desorption to improve the surface quality and uniformity by removing residues from the substrate surfaces. After that 200 nm of n+ metal rich GaN was grown at $740°\text{C}$ using a Ga beam equivalent pressure of 6.4×10^{-7} Torr to ensure a smooth and clean surface. The excess Ga was desorbed every 17 minutes by closing the Ga shutter while keeping the nitrogen shutter open until a bright and streaky RHEED pattern was observed (24).

After the n^+ GaN growth, 200 nm of $Sc_{0.27}Al_{0.73}N$ was grown under N-rich conditions, which are beneficial to improve phase purity and surface roughness. The Sc composition is accurate to ±1%. The growth temperature of ScAlN was 750 °C. Figure 1 shows a schematic of the structure. The bandgap of the ScAlN at this composition is 5.1eV (25, 26). We did not employ x-ray photoelectron spectroscopy (XPS) to determine the band gap of the ScAlN by looking at the energy loss region of the lattice elements because both the Sc and Al have spin-orbit splitting which makes it difficult to determine the 'zero' point. Also, the N 1s peak was too close to the Sc peak, overlapping the onset of inelastic losses.

A Veeco Dimension ICON atomic force microscopy (AFM) was employed to characterize the surface morphology of the samples. A smooth surface morphology with rms roughness ~0.74nm has been obtained for the ScAlN film as shown in the $2\mu\text{m} \times 2\mu\text{m}$ AFM image on Figure 2. High-resolution x-ray diffraction (HRXRD) ω-2θ scan of the sample was recorded on Rigaku Smartlab XRD. The XRD plot presented in Figure 3 clearly shows the GaN and the ScAlN peaks. This also confirms the pure wurtzite phase of ScAlN present in the samples. The second peak close to ScAlN peak can be attributed to AlN buffer layer present in the substrate. Figure 4 shows the energy dispersive spectroscopy (EDS) spectra of ScAlN film measured in Hitachi SU8000 scanning electron microscope (SEM). The EDS shows 26% Sc in the ScAlN sample. However, 27% Sc has been obtained from secondary ion mass spectrometry (SIMS) of a ScAlN thin film grown in similar growth condition.

To measure band alignments of SiO_2 or Al_2O_3 on the ScAlN, these dielectrics were deposited by two different methods, rf magnetron sputtering or ALD. The deposition conditions have been described previously (27). In brief, the sputtering was performed near room temperature with pure Si or Al targets in a 3%O_2/Ar ambient. The ALD layers for both dielectrics were deposited at 200°C using trimethylaluminum or tris (diethylamino) silane as precursors, respectively, for SiO_2 or Al_2O_3. The bandgaps of the dielectrics were 8.7 eV for ALD SiO_2 and 8.3 eV for sputtered SiO_2 and 6.3 eV for Al_2O_3 deposited by either method. These were determined by reflection electron energy loss spectroscopy (REELS) and by the O1s peak from the reference dielectric data and were consistent with those reported previously (27). Thus, subsequent differences in conduction band offsets were not due to differences in the Al_2O_3 bandgaps deposited by the two methods but were affected in the case of SiO_2. Both thick (200 nm) and thin (1.5 nm) layers of the SiO_3 or Al_2O_3 were deposited for measuring their bandgaps and core levels for these layers on the ScAlN. REELS an advantage over UV/Vis since it only requires the film to be at least as thick as the sampling depth, which is typically a few nanometers. In addition, most UV/Vis systems have a cutoff at ~6eV, but REELS does not have such an energy restriction.

XPS performed with a Physical Instruments ULVAC PHI system was used to obtain valence band offsets with the standard method of Kraut (28), employing an Al X-ray source (energy 1486.6 eV) with source power 300W, analysis size of 20 μm diameter, a take-off angle of 50◦ and an acceptance angle of ± 7 degrees. the electron pass energy was 23.5 eV for high-resolution scans and 93.5 eV for survey scans. The total energy resolution of this XPS system is about 0.5 eV, and the accuracy of the observed binding energy is within 0.03 eV.

Results and Discussion

To measure the band alignment using the Kraut method, three samples are needed. First, precise core level and valence band edge data must be measured from thick samples of the ScAlN and also both dielectrics under investigation (28-30). Then, the same core level locations measured in these bulk samples are re-measured within a heterostructure of SiO_2/ ScAlN and Al_2O_3/ ScAlN. The shift of the core level binding energy locations within the heterostructures as compared to the initial bulk binding energies can be used to determine the respective valence band offsets (28-30). Figure 5 shows the high-resolution valence band maximum (VBM)-core delta region in ScAlN. We used the Sc peak for both SiO_2 and Al_2O_3 band alignment. Similarly, high resolution XPS spectra of the valence band maximum (VBM)-core delta region are shown in Figure 6 for the sputtered and ALD SiO_2 (top) and for the corresponding Al_2O_3 cases (bottom).

The REELS spectra for all the thick dielectrics are shown in Figure 7. The dielectric band gap is obtained from the onset of the electron energy loss spectra. The energy where the onset of inelastic losses occurs is obtained by extrapolating the linear-fit line and calculating its intersection with the “zero” level. The band gap is the difference between the centroid of elastic scattering and the calculated intersection. As shown in Figure 7, while the bandgaps of the Al_2O_3 films are independent of the deposition method, there is a difference of 0.3 eV for the SiO_2.

Figure 8 shows the XPS spectra for the ScAlN to (top) sputtered SiO_2 and ALD SiO_2 and to (bottom) sputtered and ALD Al_2O_3 core delta regions in the heterostructure samples. These values are summarized in Table I and were used to calculate the valence band offsets for the different structures used in this study (31). The separation between the reference core levels can be translated directly into a value for the valence band offsets (VBOs) using the previously measured single layer sample core-level to valence band maximum (VBM) energies. There are shifts of 0.4-0.5 eV in the VBO from sputtered to ALD dielectrics in each case. This is commonly observed in these dielectrics on other materials, showing the effect of the deposition method on the VBO, which is directly measured and not derived from other measurements. As suggested previously (29), the valence band offset can be changed by modification of the interface between the sputtered dielectrics and the ScAlN. In the case of sputter deposition, it is highly likely that the impingement of energetic ions during the process can cause changes at this interface, compared to the more benign environment of ALD. The ion energies during sputtering are up to ~500 eV, well above the threshold for atomic displacements to occur in the ScAlN. Another possible source of interfacial changes would be metallic contamination during the sputtering process, originating from the electrodes in the chamber. However, the XPS data did not show any presence of metallic contamination in the dielectric films deposited by either sputtering or ALD. The VBO at the interfaces of the latter with ScAlN are probably the normal values.   It will be interesting to measure interlace state densities in capacitor structures to quantitatively establish the difference between the two types of deposition on ScAlN. Clearly, however, ALD appears to be a better choice for dielectric deposition on this material relative to sputtering.

Having measured the VBOs and bandgaps, we then derived the conduction band offsets from these values. Figures 9 and 10 shows the band alignment for the $SiO_2/Sc_{0.27}Al_{0.73}N$ heterostructure in which the SiO_2 was deposited by sputtering (Figure 9) or ALD (Figure 10).

Both are nested type I alignments. There is a difference of 0.5 eV in the VBOs and 0.1 eV in the conduction band offsets (CBOs) between the two deposition methods. Both the VBO and CBO are > 1eV, which is a rule-of-thumb for having effective carrier confinement of both electrons and holes in electronic devices. In our experience, the SiO_2 can be selectively removed from the ScAlN with standard buffered oxide etches, and F_2-based plasma etching, so these are advantages from a practical device processing view.

Similar results for the Al_2O_3/ScAlN heterostructures are shown in Figure 11 for the sputtered dielectric and Figure 12 for the ALD dielectric. These are type II, staggered alignments. However, while the VBOs are 1.5 eV, the CBOs are small, between 0.3 and 0.7 eV, which means electron confinement would not be as effective as hole confinement. The Al_2O_3 can also be selectively removed from the ScAlN by the same wet and dry processes for SiO_2. Given the larger CBOs for SiO_2, it appears this is a superior choice as a dielectric on ScAlN for electronic device applications

Summary and Conclusions

In device designs that utilize a gate dielectric, one of the most crucial parameters for the dielectric/semiconductor system of interest is that the dielectric acts as a barrier to both holes and electrons to prevent leakage current. SiO_2 has type I band alignments while Al_2O_3 has type II band alignments on a composition of ScAlN (27 at % Sc) typical of actuator and rf transistor applications and both would provide good carrier confinement. We find that there is a significant difference in valence band offsets between dielectrics deposited by sputtering compared to ALD. This has been observed in other ultra-wide bandgap materials and indicates these semiconductors are susceptible to surface disorder during sputtering (29,30).

Acknowledgments

The authors would like to thank the Research Service Center (RSC) staff at the University of Florida for their help in the fabrication and characterization of these materials. The work at UF was performed as part of Interaction of Ionizing Radiation with Matter University Research Alliance (IIRM-URA*)*, sponsored by the Department of the Defense, Defense Threat Reduction Agency under award HDTRA1-20-2-0002. The content of the information does not necessarily reflect the position or the policy of the federal government, and no official endorsement should be inferred. The work at UF was also supported by NSF DMR 1856662 (James Edgar). The work at UMichigan was supported by Naval Research Office under Contract N00014-19-1-2225. The authors would like to thank Cindy Lee for the AFM and XRD.

AUTHOR DECLARATIONS

Conflict of Interest

The authors have no conflicts to disclose.

DATA AVAILABILITY

The data that support the findings of this study are available from the corresponding author upon reasonable request.

References

1. S. Fichtner, N. Wolff, F. Lofink, L. Kienle, and B. Wagner, J. Appl. Phys., 125, 114103 (2019).

2. Ping Wang, Ding Wang, Boyu Wang, Subhajit Mohanty, Sandra Diez, Yuanpeng Wu, Yi Sun, Elaheh Ahmadi, and Zetian Mi, Appl. Phys. Lett. 119, 082101 (2021).

3. Joseph Casamento, Hyunjea Lee, Takuya Maeda, Ved Gund, Kazuki Nomoto, Len van Deurzen, Wesley Turner, Patrick Fay, Sai Mu, Chris G. Van de Walle, Amit Lal, Huili (Grace) Xing, and Debdeep Jena, Appl. Phys. Lett. 120, 152901 (2022).

4. Christian Manz, Stefano Leone, Lutz Kirste, Jana Ligl, Kathrin Frei, Theodor Fuchs, Mario Prescher, Patrick Waltereit, Marcel A Verheijen, Andreas Graff, Michél Simon-Najasek, Frank Altmann, Michael Fiederle and Oliver Ambacher, Semicond. Sci. Technol. 36, 034003 (2021).

5. Jana Ligl, Stefano Leone, Christian Manz, Lutz Kirste, Philipp Doering, Theodor Fuchs, Mario Prescher, and Oliver Ambacher, J. Appl. Phys.127, 195704 (2020)

6. W. B. Wang, Y. Q. Fu, J. J. Che, W. P. Xuan, J. K. Chen, X. Z. Wang, P. Mayrhofer, P. F. Duan, A. Bittner, U. Schmid and J. K. Luo, J. Micromech. Microeng. 26. 075006 (2016).

7. M. Akiyama, T. Kamohara, K. Kano, A. Teshigahara, Y. Takeuchi, and N. Kawahara, Adv. Mater., 21, 593 (2009).

8. V. Gund, Benyamin Davaji, Hyunjea Lee, M.J. Asadi, Joseph Casamento, Huili Grace Xing, Debdeep Jena and Amit Lal, “Temperature-dependent Lowering of Coercive Field in 300 nm Sputtered Ferroelectric $Al_{0.70}Sc_{0.30}N$,” IEEE Int. Symp. Appl. Feeroelectric, ISAF 2021, Int. Symp. Integr. Funct. ISIF 2021, Piezoresponse Force Microsc. Work. PFM 2021 - Proc., May 2021.

9. V. Gund, Benyamin Davaji, Hyunjea Lee, Joseph Casamento, Huili Grace Xing, Debdeep Jena and Amit Lal, "Towards Realizing the Low-Coercive Field Operation of Sputtered Ferroelectric $Sc_xAl_{1-x}N$," 21st Int. Conf. Solid-State Sensors, Actuators Microsystems, Transducers 2021, pp. 1064– 1067, Jun. 2021

10. B. Herrera, M. Pirro, G. Giribaldi, L. Colombo, and M. Rinaldi, "AlScN Programmable Ferroelectric Micromachined Ultrasonic Transducer (FMUT)," 21st Int. Conf. Solid-State Sensors, Actuators Microsystems, Transducers 2021, pp. 38–41, Jun. 2021,

11. S. Dabas, D. Mo, S. Rassay, and R. Tabrizian, "Intrinsically Tunable Laminated Ferroelectric Scandium Aluminum Nitride Extensional Resonator Based on Local Polarization Switching," IEEE Symp. Mass Storage Syst. Technol., vol. 2022-January, pp. 1050 (2022).

12. Z. Tang, M. D'Agati, and R. H. Olsson, "High Coupling Coefficient Resonance Mode in $Al_{0.68}Sc_{0.32}N$ Surface Acoustic Wave Resonator with AlN Buffer Layer on a Silicon Substrate," IFCS-ISAF 2020 - Jt. Conf. IEEE Int. Freq. Control Symp. IEEE Int. Symp. Appl. Ferroelectr. Proc., Jul. 2020.

13. Z. Hao, Mingyo Park, Dea Gyu Kim, Andrew Clark Rytis Dargis, Haoshen Zhu and A. Ansari, Single Crystalline ScAlN Surface Acoustic Wave Resonators with Large Figure of Merit (Q × k)," IEEE MTT-S Int. Microw. Symp. Dig., vol. 2019-June, pp. 786–789, Jun. 2019.

14. J. Wang, M. Park, S. Mertin, T. Pensala, F. Ayazi, and A. Ansari, "A Film Bulk Acoustic Resonator Based on Ferroelectric Aluminum Scandium Nitride Films," J. Microelectromechanical Syst., 29, 741 (2020).

15. Ved Gund, Kazuki Nomoto, Huili Grace Xing, Debdeep Jena and Amit Lal, Intrinsically Switchable GHz Ferroelectric ScAlN SAW Resonators, 2022 IEEE International Symposium on Applications of Ferroelectrics (ISAF).

16. Ding Wang, Ping Wang, Shubham Mondal, Subhajit Mohanty, Tao Ma, Elaheh Ahmadi, and Zetian Mi, Adv. Electron. Mater. 8, 2200005 (2022)

17. F. Tasnádi, B. Alling, C. Höglund, G. Wingqvist, J. Birch, L. Hultman and I.A. Abrikosov, Phys. Rev. Lett. 104 137601 (2010)

18. C. Tholander, I. Abrikosov, L. Hultman and F. Tasnádi, Phys. Rev. B 87, 094107 (2013).

19. Joseph Casamento, Celesta S. Chang, Yu-Tsun Shao, John Wright, David A. Muller, Huili (Grace) Xing, and Debdeep Jena, Appl. Phys. Lett. 117, 112101 (2020).

20. M. T. Hardy, B. P. Downey, N. Nepal, D. F. Storm, D. S. Katzer, and D. J. Meyer, Appl. Phys. Lett., vol. 110, p. 162104, 2017.

21. T.E. Kazior, E, M. Chumbes, B. Schultz, J. Logan, D.J. Meyey and M.T. Hardy, 2019 IEEE MTT-S International Microwave Symposium (IMS 2019) (2–7 June 2019 Boston, MA) (Piscataway, NJ: IEEE)1136–9

22. A.J. Green, James K. Gillespie, Robert C. Fitch Jr., Dennis E. Walker Jr., Miles Lindquist, Antonio Crespo, Dan Brooks, Edward Beam, Andy Xie, Vipan Kumar, Jose Jimenez, Cathy Lee, Yu Cao, Kelson D. Chabak and Gregg H. Jessen, IEEE Electron Device Lett. 40, 1056 (2019).

23. A. J. Green, Neil Moser, Nicholas C. Miller, Kyle J. Liddy, Miles Lindquist, Michael Elliot, James K. Gillespie, Robert C. Fitch, Jr., Ryan Gilbert, Dennis E. Walker, Jr., Elizabeth Werner, Antonio Crespo, Edward Bea, Andy Xie, Cathy Le, Yu Cao and Kelson D. Chabak, IEEE Electron Device Lett. 41, 1181 (2020).

24. K. Hestroffer, C. Lund, O. Koksaldi, H. Li, G. Schmidt, M. Trippel, P. Veit, F. Bertram, N. Lu, Q. Wang, J. Christen, M. J. Kim, U. K. Mishra, and S. Keller, J. Cryst. Growth 465, 55 (2017).

25. Martina Baeumler, Yuan Lu, Nicolas Kurz, Lutz Kirste, Mario Prescher, Tim Christoph, Joachim Wagner, Agnė Žukauskaitė, and Oliver Ambacher, J. Appl. Phys 126, 045715 (2019).

26. Ruopeng Deng, Sarah R. Evans, and Daniel Gall, Appl. Phys. Lett. 102, 112103 (2013).

27. Chaker Fares F. Ren, David C. Hays, B. P. Gila and S. J. Pearton, ECS J. Solid State Sci. Technol. 8, Q3001 (2019).

28. E. A. Kraut, R. W. Grant, J. R. Waldrop, and S. P. Kowalczyk, Phys. Rev. Lett., 44,1620 (1980).

29. D. C. Hays, B. P. Gila, S. J. Pearton, and F. Ren, Appl. Phys. Rev., 4, 021301 (2017).

30. Chaker Fares, F. Ren, Eric Lambers, David C. Hays, B. P. Gila, and S. J. Pearton, J. Vac. Sci. Technol., B36, 061207 (2018).

31. George H. Major, Vincent Fernandez, Neal Fairley, Emily F. Smith, and Matthew R. Linford, J. Vac. Sci. Technol. A 40, 063201 (2022).

Table 1. Summary of measured core levels in these experiments (eV). The referenced core levels are Si 2p for the sputtered and ALD SiO_2. Error ranges are ~15% in each entry.

ScAlN (27%Sc)				**Reference SiO_2**			**Thin SiO_2 on ScAlN**			
VBM	Core Level Peak (Sc 2p)	Core-VBM	Film	VBM	Core Level Peak (Si 2p)	Core-VBM	Core Level Peak (Sc 2p)	Core Level Peak (Si 2p)	△Core level	Valence band offset
-0.6	397.8	398.4	Sputt. SiO_2	4.8	103.5	98.7	398.7	101.1	297.6	2.1
			ALD SiO_2	5.7	104.3	98.6	398.8	101.6	297.2	2.6

ScAlN (27%Sc)				**Reference Al_2O_3**			**Thin Al_2O_3 on ScAlN**			
VBM	Core Level Peak (Sc 2p)	Core-VBM	Film	VBM	Core Level Peak (Al 2p)	Core-VBM	Core Level Peak (Sc 2p)	Core Level Peak (Al 2p)	△Core level	Valence band offset
-0.6	397.8	398.4	Sputt. Al_2O_3	1.6	72.8	71.2	398.2	72.5	325.7	1.5
			ALD Al_2O_3	1.1	72.3	71.2	398.2	72.9	325.3	1.9

Figure Captions

Figure 1 Schematic of ScAlN structure.

Figure 2. AFM image (2µm×2µm) of $Sc_{0.27}Al_{0.73}N$ film grown at $750°C$.

Figure 3. High resolution XRD plot of $Sc_{0.27}Al_{0.73}N$.

Figure 4. EDS Spectra of ScAlN.

Figure 5. High resolution XPS spectra for the vacuum-core delta regions of $Sc_{0.27}Al_{0.73}N$.

Figure 6. High resolution XPS spectra for the vacuum-core delta regions of (top) sputtered SiO_2 compared to (bottom) ALD SiO_2. The intensity is in arbitrary units (a.u.).

Figure 7. REELS spectra for sputtered and ALD SiO_2 (top) and sputtered and ALD Al_2O_3 (bottom).

Figure 8. High resolution XPS spectra for the ScAlN to (top) sputtered SiO_2 and (bottom) ALD SiO_2 core delta regions. The intensity is in arbitrary units (a.u.).

Figure 9. Band diagram for sputtered SiO_2 on $Sc_{0.27}Al_{0.73}N$.

Figure 10. Band diagram for ALD SiO_2 on $Sc_{0.27}Al_{0.73}N$.

Figure 11. Band diagram for sputtered Al_2O_3 on $Sc_{0.27}Al_{0.73}N$.

Figure 12. Band diagram for ALD Al_2O_3 on $Sc_{0.27}Al_{0.73}N$.

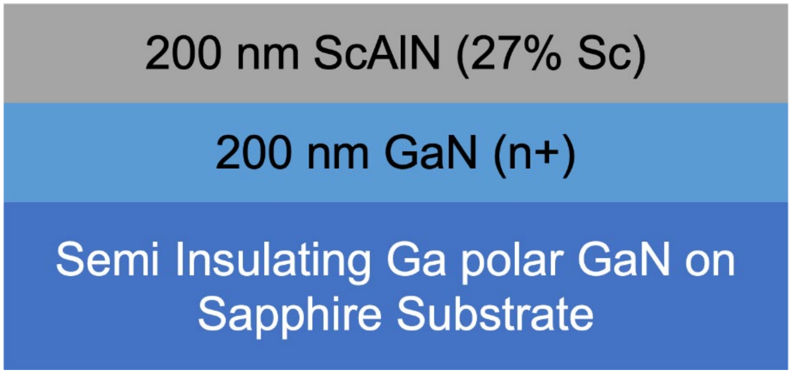
200 nm ScAlN (27% Sc)
200 nm GaN (n+)
Semi Insulating Ga polar GaN on Sapphire Substrate

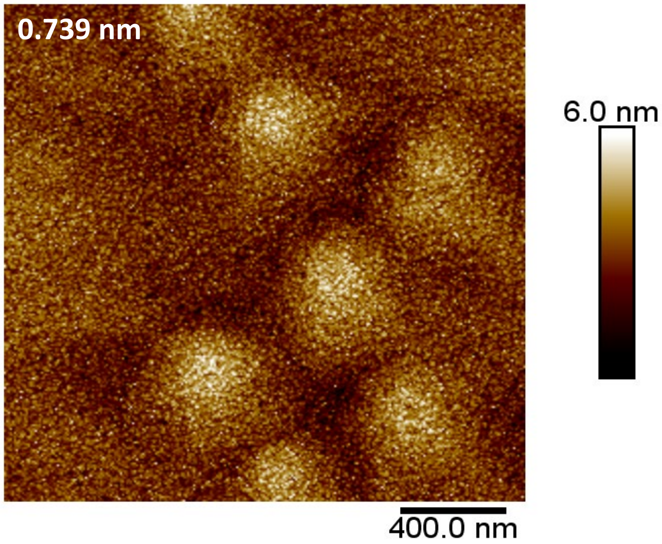
0.739 nm
6.0 nm
400.0 nm

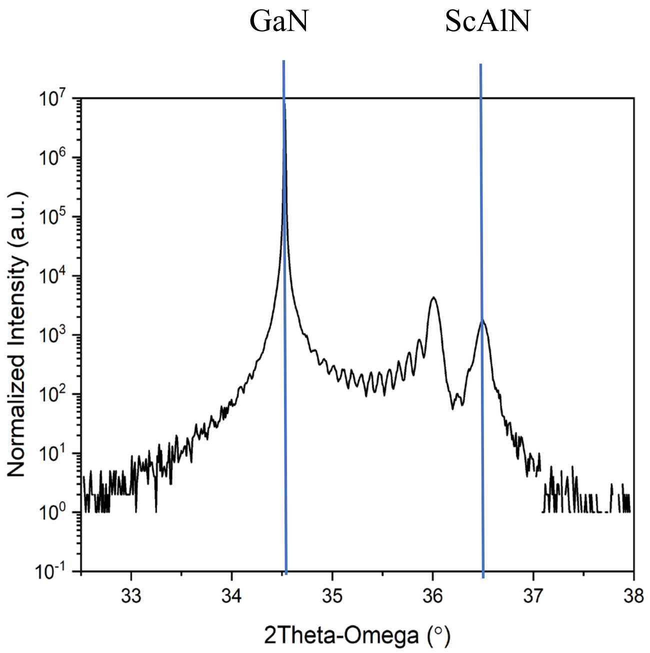
GaN
ScAlN
Normalized Intensity (a.u.)
10^{7}
10^{6}
10^{5}
10^{4}
10^{3}
10^{2}
10^{1}
10^{0}
10^{-1}
33
34
35
36
37
38
2Theta-Omega (°)

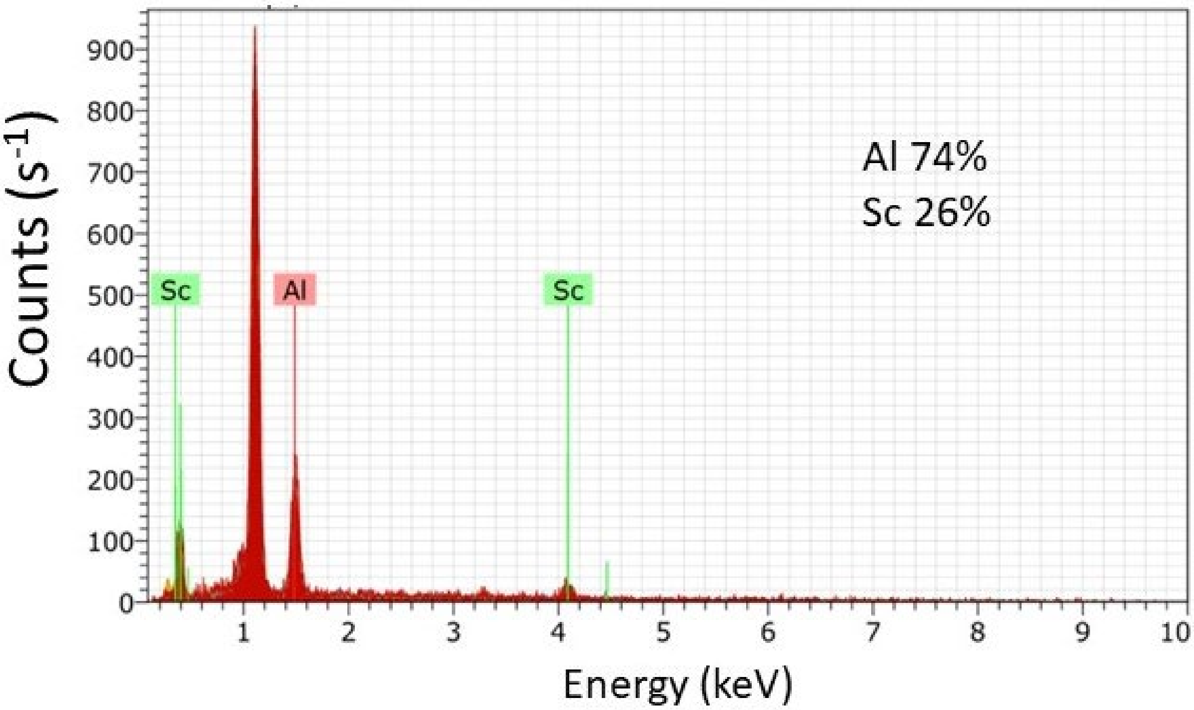
Counts (s^{-1})
900
800
700
600
500
400
300
200
100
0
Sc
Al
Sc
Al 74%
Sc 26%
1
2
3
4
5
6
7
8
9
10
Energy (keV)

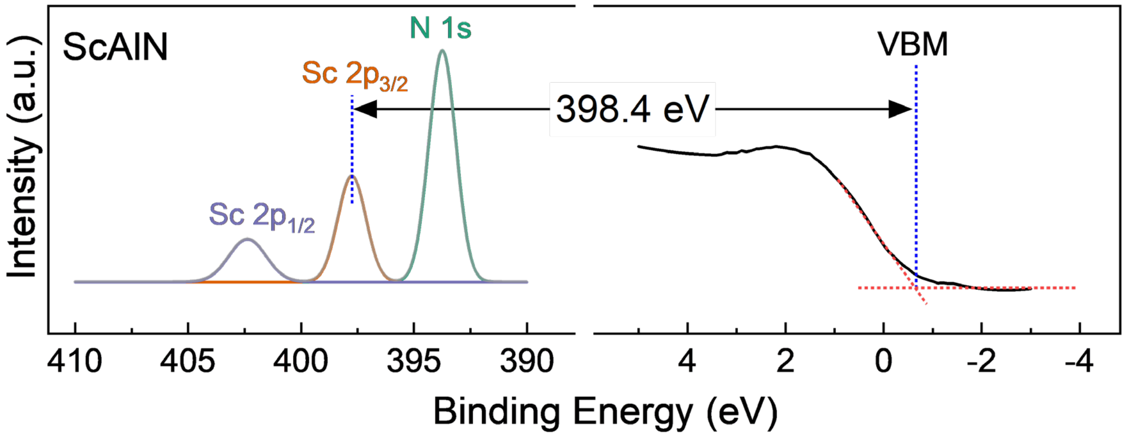
ScAlN
N 1s
Sc 2p$_{3/2}$
Sc 2p$_{1/2}$
398.4 eV
VBM
Intensity (a.u.)
410
405
400
395
390
4
2
0
-2
-4
Binding Energy (eV)

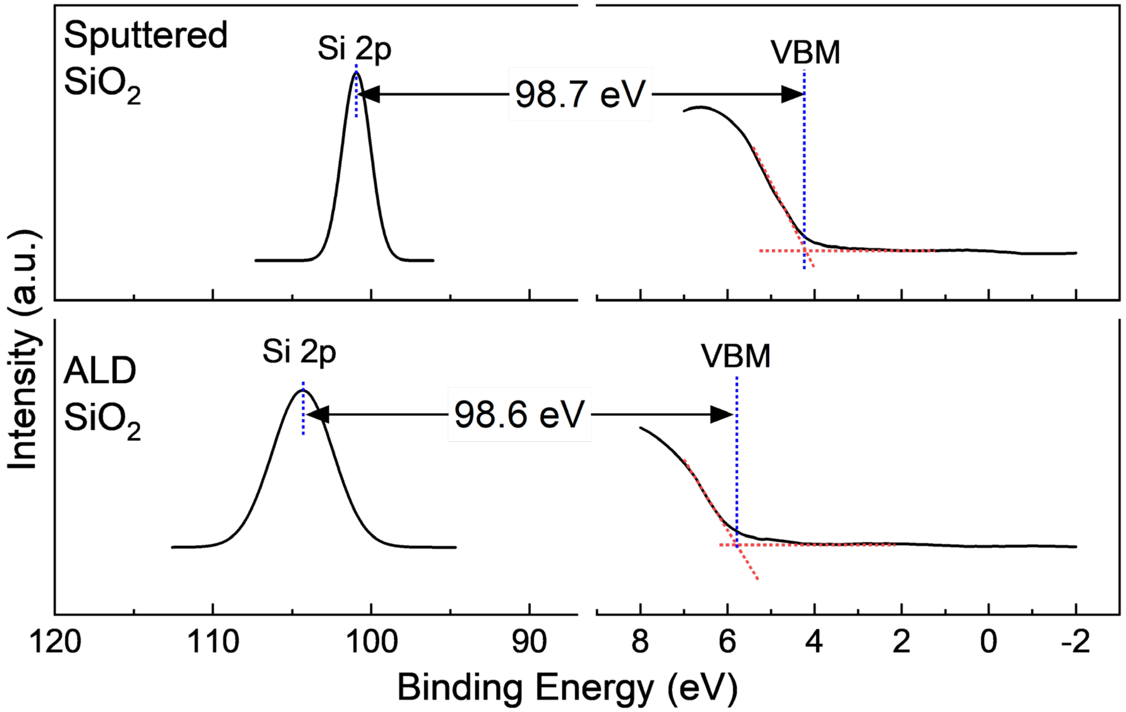
Sputtered
SiO_2
Si 2p
98.7 eV
VBM
ALD
SiO_2
Si 2p
98.6 eV
VBM
Intensity (a.u.)
120
110
100
90
8
6
4
2
0
-2
Binding Energy (eV)

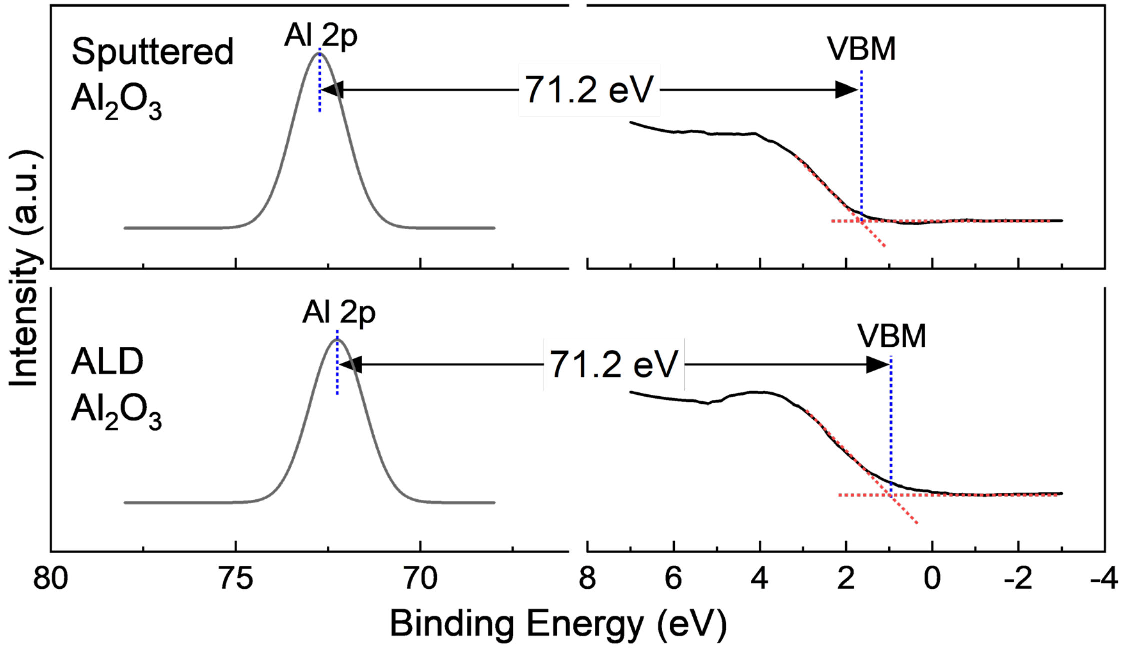
Sputtered
Al_2O_3
Al 2p
71.2 eV
VBM
ALD
Al_2O_3
Al 2p
71.2 eV
VBM
Intensity (a.u.)
80
75
70
8
6
4
2
0
-2
-4
Binding Energy (eV)

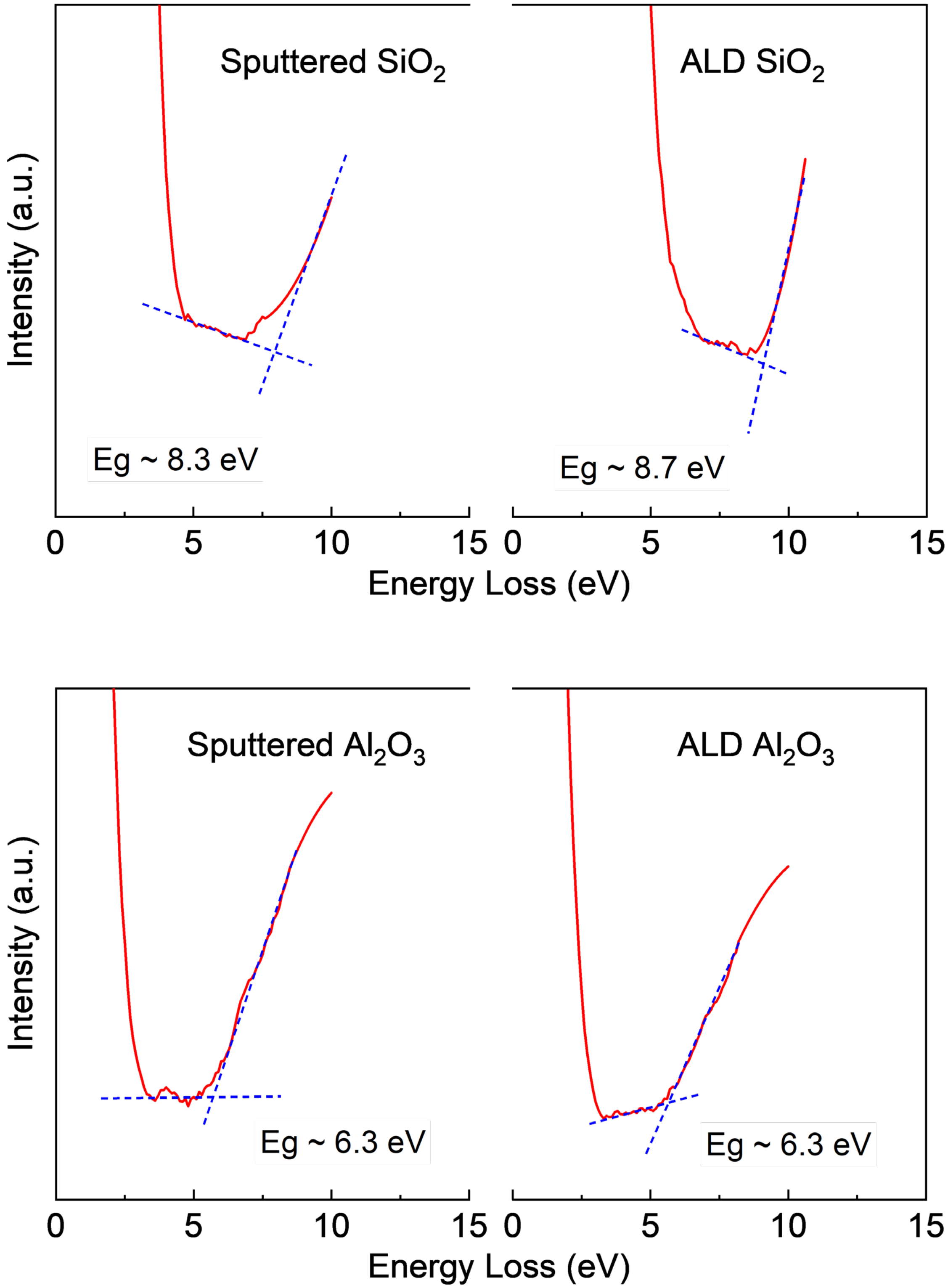
Sputtered SiO_2
ALD SiO_2
Eg ~ 8.3 eV
Eg ~ 8.7 eV
Sputtered Al_2O_3
ALD Al_2O_3
Eg ~ 6.3 eV
Eg ~ 6.3 eV
Intensity (a.u.)
Intensity (a.u.)
Energy Loss (eV)
Energy Loss (eV)
0
5
10
15
0
5
10
15

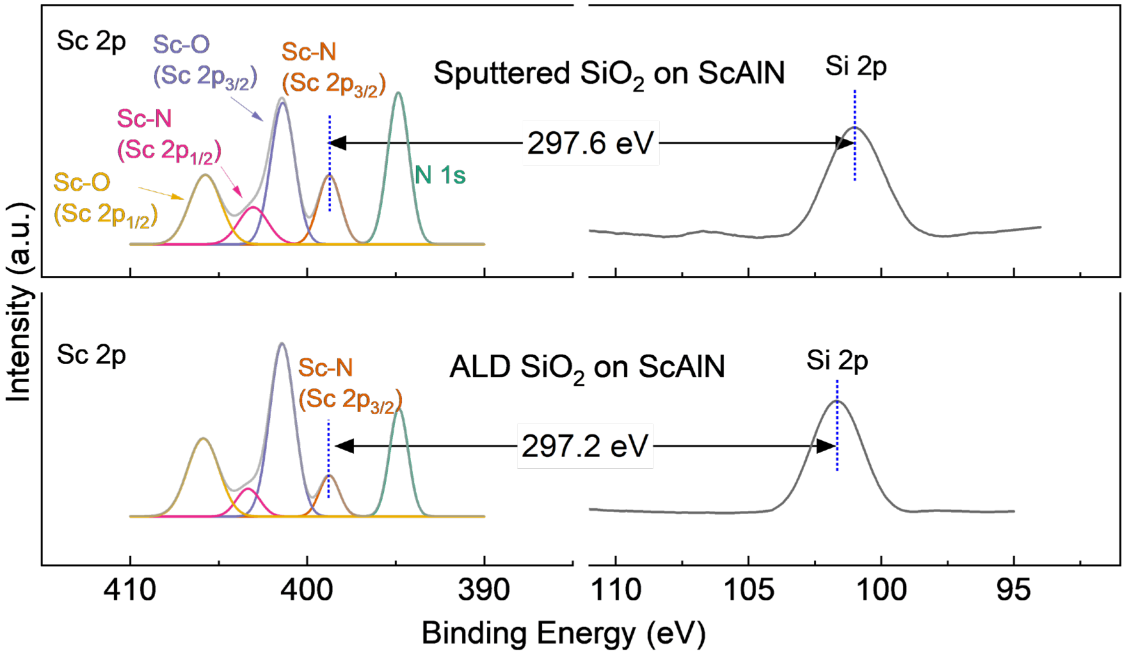
Sc 2p
Sc-O
(Sc $2p_{3/2}$)
Sc-N
(Sc $2p_{3/2}$)
Sputtered SiO_2 on ScAlN
Si 2p
Sc-N
(Sc $2p_{1/2}$)
297.6 eV
Sc-O
(Sc $2p_{1/2}$)
N 1s
Sc 2p
Sc-N
(Sc $2p_{3/2}$)
ALD SiO_2 on ScAlN
Si 2p
297.2 eV
Intensity (a.u.)
410
400
390
110
105
100
95
Binding Energy (eV)

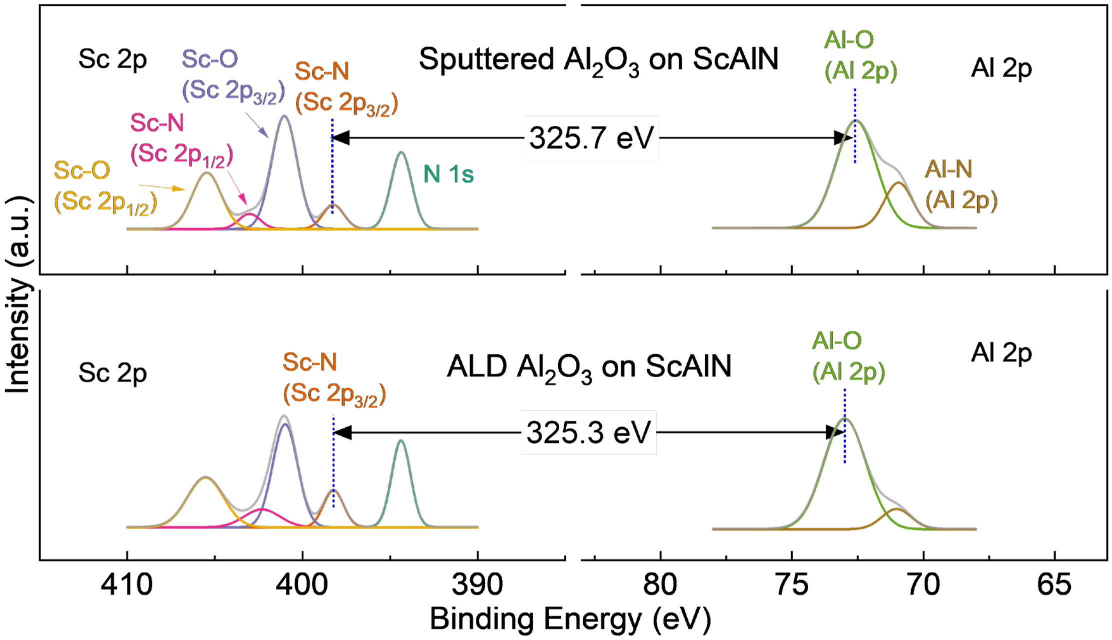
Sc 2p
Sc-O
(Sc $2p_{3/2}$)
Sc-N
(Sc $2p_{3/2}$)
Sputtered Al_2O_3 on ScAlN
Al-O
(Al 2p)
Al 2p
Sc-N
(Sc $2p_{1/2}$)
325.7 eV
Sc-O
(Sc $2p_{1/2}$)
N 1s
Al-N
(Al 2p)
Sc 2p
Sc-N
(Sc $2p_{3/2}$)
ALD Al_2O_3 on ScAlN
Al-O
(Al 2p)
Al 2p
325.3 eV
Intensity (a.u.)
410
400
390
80
75
70
65
Binding Energy (eV)

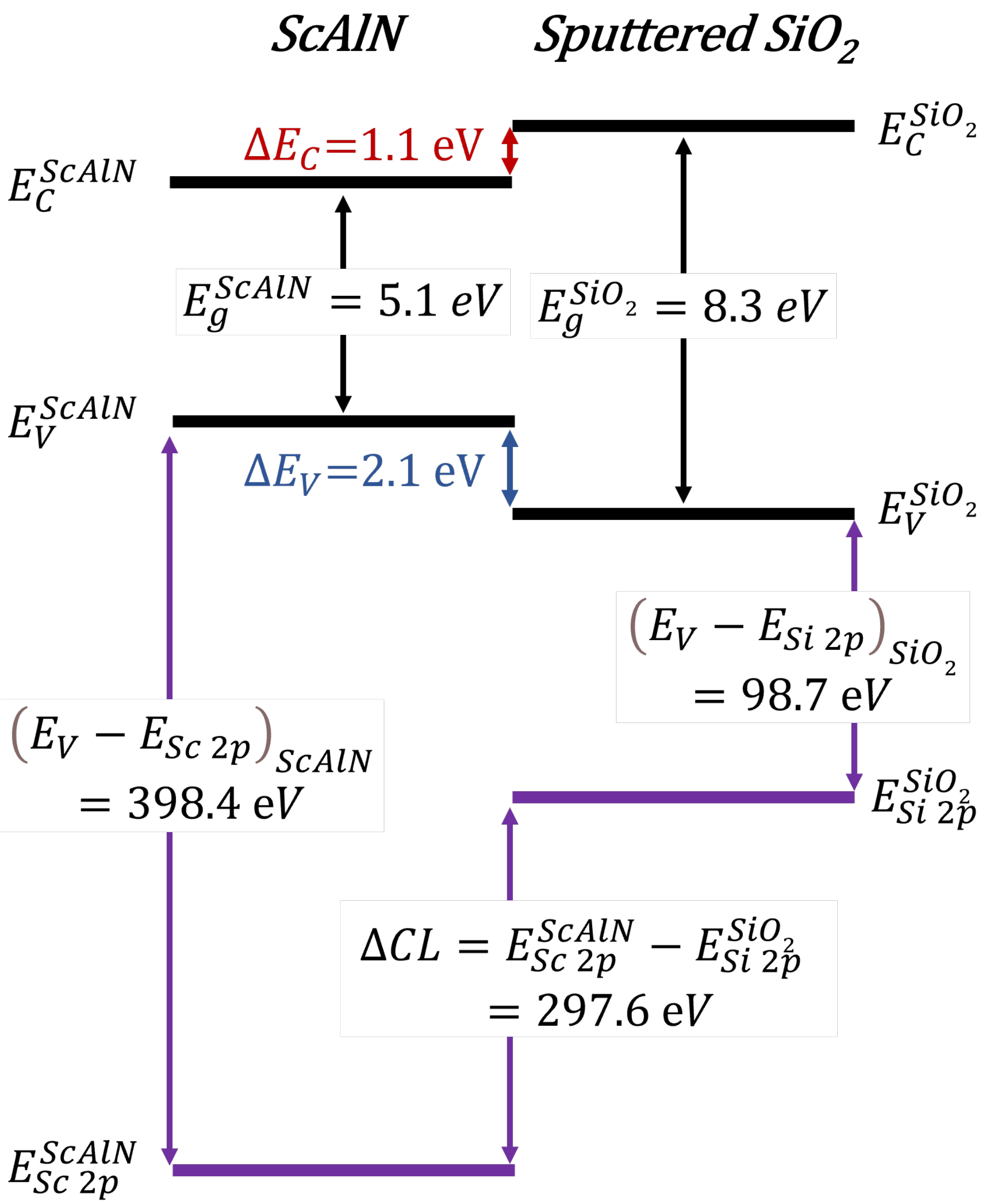
ScAlN
Sputtered SiO_2
E_C^{ScAlN}
ΔE_C=1.1 eV
$E_C^{SiO_2}$
$E_g^{ScAlN} = 5.1\ eV$
$E_g^{SiO_2} = 8.3\ eV$
E_V^{ScAlN}
ΔE_V=2.1 eV
$E_V^{SiO_2}$
$(E_V - E_{Si\ 2p})_{SiO_2} = 98.7$ eV
$(E_V - E_{Sc\ 2p})_{ScAlN} = 398.4$ eV
$E_{Si\ 2p}^{SiO_2}$
$\Delta CL = E_{Sc\ 2p}^{ScAlN} - E_{Si\ 2p}^{SiO_2} = 297.6$ eV
$E_{Sc\ 2p}^{ScAlN}$

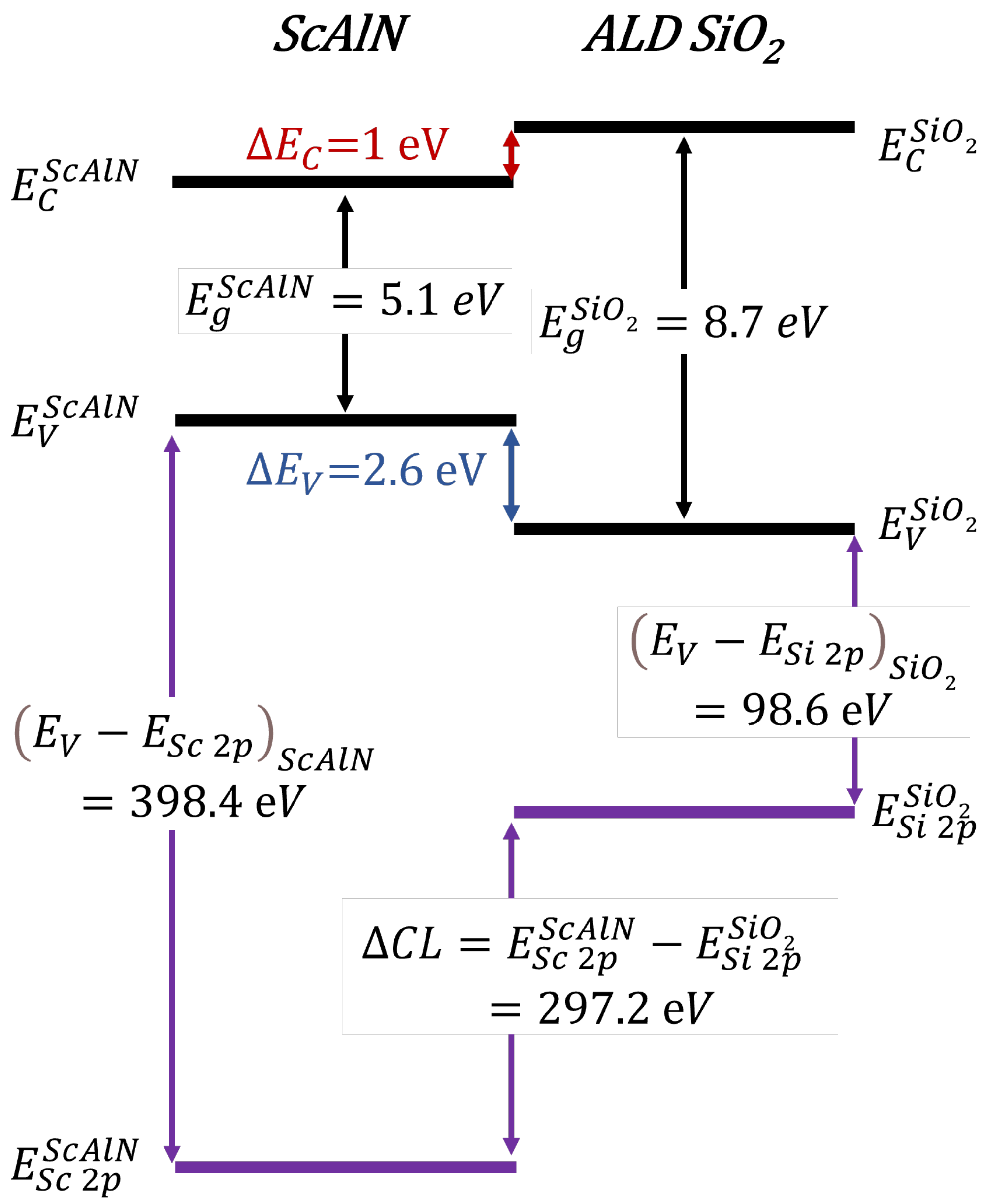
ScAlN
ALD SiO_2
ΔE_C=1 eV
E_C^{ScAlN}
$E_C^{SiO_2}$
$E_g^{ScAlN} = 5.1\ eV$
$E_g^{SiO_2} = 8.7\ eV$
E_V^{ScAlN}
ΔE_V=2.6 eV
$E_V^{SiO_2}$
$(E_V - E_{Si\ 2p})_{SiO_2} = 98.6\ \mathrm{eV}$
$(E_V - E_{Sc\ 2p})_{ScAlN} = 398.4\ \mathrm{eV}$
$E_{Si\ 2p}^{SiO_2}$
$\Delta CL = E_{Sc\ 2p}^{ScAlN} - E_{Si\ 2p}^{SiO_2} = 297.2\ \mathrm{eV}$
$E_{Sc\ 2p}^{ScAlN}$

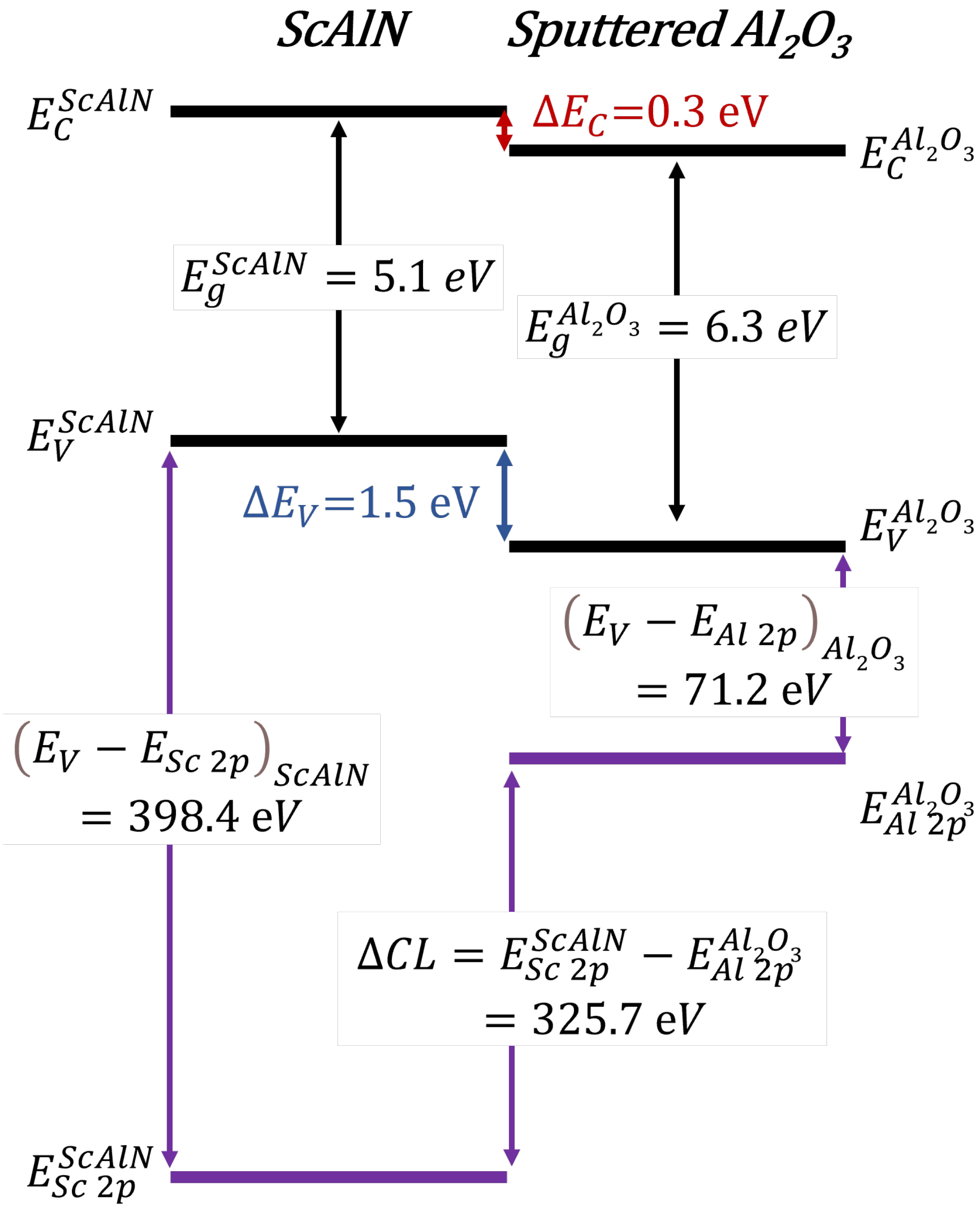
ScAlN
Sputtered Al_2O_3
E_C^{ScAlN}
ΔE_C=0.3 eV
$E_C^{Al_2O_3}$
$E_g^{ScAlN} = 5.1\ eV$
$E_g^{Al_2O_3} = 6.3\ eV$
E_V^{ScAlN}
ΔE_V=1.5 eV
$E_V^{Al_2O_3}$
$\left(E_V - E_{Al\ 2p}\right)_{Al_2O_3} = 71.2\ \text{eV}$
$\left(E_V - E_{Sc\ 2p}\right)_{ScAlN} = 398.4\ \text{eV}$
$E_{Al\ 2p}^{Al_2O_3}$
$\Delta CL = E_{Sc\ 2p}^{ScAlN} - E_{Al\ 2p}^{Al_2O_3} = 325.7\ \text{eV}$
$E_{Sc\ 2p}^{ScAlN}$

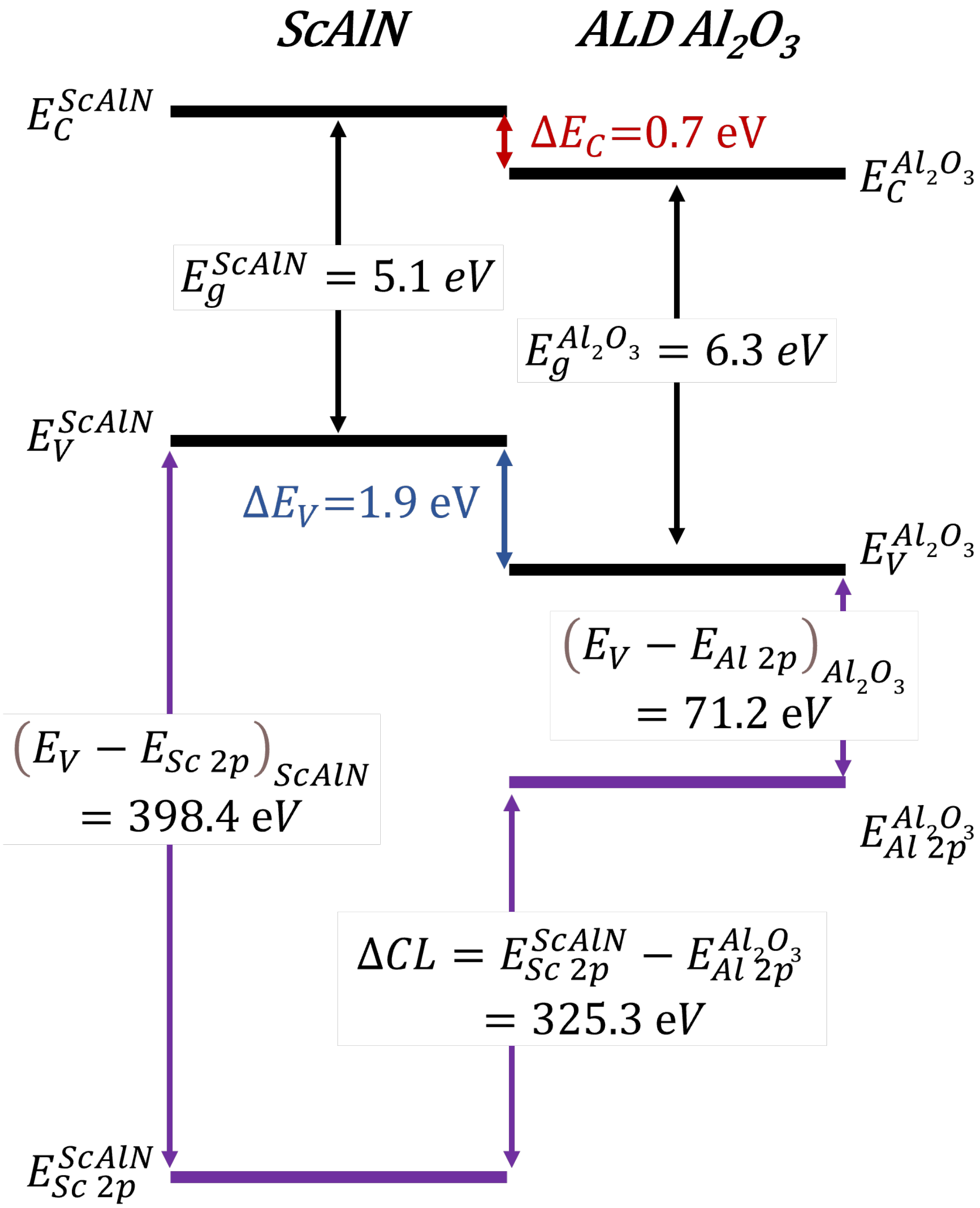
ScAlN
ALD Al_2O_3
E_C^{ScAlN}
ΔE_C=0.7 eV
$E_C^{Al_2O_3}$
$E_g^{ScAlN} = 5.1\ eV$
$E_g^{Al_2O_3} = 6.3\ eV$
E_V^{ScAlN}
ΔE_V=1.9 eV
$E_V^{Al_2O_3}$
$\left(E_V - E_{Al\ 2p}\right)_{Al_2O_3} = 71.2$ eV
$\left(E_V - E_{Sc\ 2p}\right)_{ScAlN} = 398.4$ eV
$E_{Al\ 2p}^{Al_2O_3}$
$\Delta CL = E_{Sc\ 2p}^{ScAlN} - E_{Al\ 2p}^{Al_2O_3} = 325.3$ eV
$E_{Sc\ 2p}^{ScAlN}$